1

2　Revision 1

3

4　Wave vector and field vector orientation dependence of Fe K pre-edge X-ray absorption features

5　in clinopyroxenes

6

7

8　Cody J. Steven[1], M. Darby Dyar[1,2], Molly McCanta[3], Matthew Newville[4], and Antonio

9　Lanzirotti[4]

10

11

12　[1]Planetary Science Institute, Tucson, Arizona 85719-2395, U.S.A.

13

14　[2]Department of Astronomy, Mount Holyoke College, South Hadley, Massachusetts 01075,

15　U.S.A.

16

17　[3]Department of Earth and Planetary Sciences, University of Tennessee, Knoxville, Tennessee

18　37996, U.S.A.

19

20　[4]Center for Advanced Radiation Sources, University of Chicago, 5640 S. Ellis Avenue, Chicago,

21　Illinois 60637, U.S.A.

22

23

Abstract

Pre-edge X-ray absorption features are commonly used to derive redox states for transition metal oxides in crystals and glasses. Several calibrations for Fe^{2+} and Fe^{3+} in silicate glasses have utilized the general relationships among pre-edge peak intensity, energy, and redox state. However, absorption variations complicate those relationships in anisotropic crystals. Although absorption anisotropy at and above the energy of the rising edge adheres to the typical $\cos^2$ relationship observed in absorption spectroscopies at other energies, the anisotropy of the pre-edge is far more complicated. Prior studies focusing on pre-edge absorption anisotropy demonstrate a $1-\cos 4\phi$ dependence of absorption magnitudes with rotation. Experiments presented here show that absorption magnitudes of the pre-edge vary as a function of both electric field vector orientation and wave vector direction. However, rotations around the field vector axis or wave vector axis individually result in $\cos^2$ dependence of absorption magnitudes. Rotations where both wave vector and field vector orientation are varied are not well-fit by either model in the pre-edge. The resulting anisotropy complicates the process of measuring characteristic absorption in the pre-edge, making valence state determinations challenging for strongly anisotropic crystal structures such as pyroxene.

Introduction

In transition metal oxides, absorption over the pre-edge energy range of X-ray absorption spectra is an important indicator of oxidation state and distortion of metal-containing polyhedra. Because of its sensitivity to valence state, the pre-edge has been used by numerous authors to

47   indicate oxygen fugacity (f_{O2}) of the crystallization or solidification environment of igneous and

48   metamorphic rocks (Bajt et al., 1994; Wilke et al., 2004; Yaxley et al., 2012). Among the

49   community of X-ray absorption spectroscopy (XAS) users, absorption anisotropy of spectra

50   collected from crystals is known to be a barrier to quantifying valence states of multivalent

51   elements (Dyar et al. 2002; Muñoz et al. 2013). Research on mineral samples has shown that in

52   anisotropic materials, calibrations for quantifying multivalent elements can be profoundly

53   affected by the orientation of the photon source relative to the polarization direction of the

54   crystals being studied.

55   The angular dependence of absorption anisotropy from energies spanning from the rising

56   edge and above is closely approximated as a $\cos^2\theta$ relationship from one absorption magnitude

57   to another. This has been demonstrated by numerous authors (Heald and Stern, 1977; Rosenberg

58   et al., 1986; Stöhr and Outka, 1987) and applied as a way of empirically interpolating absorption

59   magnitudes. In this study, the $\cos^2\theta$ relationship was determined from observations made using

60   ultraviolet-visible (UV-Vis) and infrared spectroscopies, where absorption magnitudes have

61   similar anisotropies.

62   In our earlier work, Steven et al. (2022) show that absorption anisotropy is well-modeled

63   in three dimensions with a $\cos^2\theta$ absorption indicatrix, a geometric model representing

64   absorption magnitudes for a given field vector direction. However, pre-edge anisotropy was

65   distinctly discordant from the $\cos^2\theta$ model. The discrepancy was suspected to be due to the

66   nature of the quadrupole transitions at pre-edge energies coupled with the relatively low

67   absorption intensities near the intense rising edge. For example, even a slightly overabsorbed

68   scan causes pre-edge peaks to be systematically more intense than an ideal scan, and is not

69   always fully corrected for in the normalization process. The suggestion that the discordance is

70   the result of quadrupole transitions is not new. An earlier example is a model employed by Hahn

71   et al. (1982), $\sin^2 2\phi$, which interpolates the observed data in Cu K-edge scans of a $(CuCl_4)^{2-}$

72   complex. Similarly, Uozumi et al. (1992) employed an equivalent model, $1-\cos 4\phi$, to describe

73   pre-edge anisotropy of Ti K-edge spectra of TiO_2.

74   The objective of this research is to characterize the nature of absorption anisotropy in

75   clinopyroxene, with a focus on the pre-edge. Geologically, clinopyroxenes are an important

76   index mineral for determining conditions of the crystallization environment, namely in

77   geothermobarometry and oxybarometery. Among anisotropic minerals, clinopyroxenes exhibit

78   extreme X-ray absorption anisotropy, making them an ideal candidate for examining the angular

79   dependence of absorption anisotropy. Although the pre-edge peaks are the focus of these

80   experiments, full spectra were collected to gauge the extent of over-absorption. These

81   experiments were run on samples of end-member Fe^{2+} and Fe^{3+} clinopyroxenes, as well as a

82   mixed Fe^{2+}/Fe^{3+} sample.

83   **Background**

84

85   In spectra acquired over visible wavelengths, anisotropic absorption is routinely observed

86   as pleochroism on a polarized light microscope. The amount of absorption depends on absorber

87   concentration, absorber orientation, and the orientation of vibration directions in the viewing

88   section of the crystal. In other words, given a random section of a crystal, the amount of

89   absorption is first dictated by the optical indicatrix and its orientation, then by the absorption

90   indicatrix at a given wavelength. Examples of the interplay between optical and absorption

91   indicatrices are given in Libowitzky and Rossman (1996) applied to infrared spectroscopy. The

92   orientation of vibration directions can be determined if the optical indicatrix orientation is

93   known. Vibration directions are simply the semi-major and semi-minor axes of an ellipse formed

94   by a plane section across the optical indicatrix. When linearly polarized light is oriented along a

95   vibration direction, a true absorption magnitude can be acquired. Plane sections of ellipsoid

96   calculations are ubiquitous in many corners of science, but an example derivation is in Gendzwill

97   and Stauffer (1981).

98   Because absorption magnitudes are influenced by polarization, observed magnitudes can

99   vary in an irregular fashion depending on the orientation of the crystal and the rotation axis. If

100   the rotation axis is a wave vector axis, absorption magnitudes are always $\cos^2\theta$ dependent.

101   Although refraction and crystal polarization effects are nearly nonexistent for X-ray

102   wavelengths, observed absorption anisotropy over the XAS energy range shares some

103   similarities with visible light. To an extent, absorption magnitudes can be modeled in three

104   dimensions using the concept of an absorption indicatrix, where absorption magnitudes in each

105   direction are modeled by a surface-described $\cos^2$ variation in all directions, as seen on the

106   surface in Figure 1 (Steven et al., 2022). However, $\cos^2$ dependence breaks down in the pre-edge.

107   Some authors have employed microscopic models to describe the anisotropy, while others (Hahn

108   et al. 1982; Uozumi et al., 1992) have used a macroscopic $1-\cos4\phi$ model to describe magnitudes

109   from quadrupole transitions. Based on figures and descriptions of the collection geometries from

110   Hahn et al. (1982) and Uozumi et al. (1992), both collected scans from materials with rotational

111   symmetry, with that axis oriented vertically. The vertical axis was then rotated, designated in

112   both papers as a rotation of ϕ, to collect spectra at various ϕ settings. Those experiments were

113   collected in the geometry equivalent to the position shown in Figure 2, with crystals mounted

114   with rotational symmetry elements parallel to the ϕ-axis, and rotating the spindle axis ϕ. In this

115   study, θ is defined as the rotation axis parallel to the beam direction, and the ϕ-axis is defined as

116   a rotation axis orthogonal to the beam direction, which can be rotated by θ as depicted in Figure

117   2.

118   The 3-D models in Figure 1 only apply if the anisotropy depends on a single axis, such as

119   the electric field vector orientation. If there is wave vector dependence, observed absorption

120   magnitudes can deviate from these models. The experiments in this paper are designed to look

121   for and characterize this variation.

122

123   **Methods and Samples**

124

125   Three clinopyroxene samples were used to evaluate anisotropy of samples of that range

126   in $Fe^{3+}/\Sigma Fe$. They are 1) HMM119666, a hedenbergite composition from Broken Hill mines,

127   Yancowinna, New South Wales, Australia which has an $Fe^{3+}/\Sigma Fe$ of 0 and formula of

128     $(Ca_{0.990}Na_{0.002})(Fe^{2+}_{0.834}Mg_{0.045}Mn_{0.147})(Si_{1.989}Al_{0.004})O_6$ 2) DH208, an augite composition from

129   mantle xenoliths from Dish Hill, California, USA which has an $Fe^{3+}/\Sigma Fe$ of 0.36 and formula of

130     $(Ca_{0.810}Na_{0.107})(Fe^{2+}_{0.210}Fe^{3+}_{0.118}Mg_{0.579}Mn_{0.008}Al_{0.118})(Si_{1.751}Al_{0.249})O_6$ and 3) AMNH82544, an

131   aegirine from Langesundsfjord, Norway on loan from the American Museum of Natural History

132   which has an $Fe^{3+}/\Sigma Fe$ of 0.97 and formula of

133     $(Ca_{0.007}Na_{0.961})(Fe^{2+}_{0.026}Fe^{3+}_{0.849}Mg_{0.005}Mn_{0.037}Ti_{0.067}Al_{0.008})(Si_{2.013})O_6$.

134   Clinopyroxene single crystals were mounted on specimen pins with the spindle axis

135   parallel to a random axis, the **b**-axis, or the vector normal to (100). Crystal orientation was

136   guided by the (110) cleavages during mounting, then crystallographic axes vectors were located

137   using single-crystal X-ray diffraction (SC-XRD). The output orientation matrix from SC-XRD

138   was then related to the principle optical vectors using the methods described in Steven and

139   Gunter (2020).

140   For precise **b**-axis mounts, the diagonals of the intersections of the (110) cleavages were

141   mounted parallel to the specimen pin axis, resulting in an axis near either the **b**-axis, or the

142   normal vector to (100). While viewing into the microscope, the specimen pin was turned with the

143   X-ray goniometer fixed at the 0° spindle position until the long axis of the crystal (the **c**-axis)

144   was roughly in the plane of view for consistency. Crystals with an orientation matrix indicating

145   that the **b**-axis was within approximately 14° of the spindle axis are within range of goniometer

146   arc adjustments. Specimen pins on the X-ray goniometer were then marked to indicate the

147   location of the mounting notch and transferred to the coinciding position of an arc goniometer.

148   Optical orientations and crystal axes were then determined with spindle stage techniques

149   and EXCELIBR (Steven and Gunter, 2017). Despite the slight discrepancy resulting from the

150   transfer between goniometers, the crystallographic orientation from the SC-XRD should be near

151   the crystallographic orientation determined on the microscope (Figure 3). The Y = **b**-axis

152   orientation is then brought to the spindle axis by numerically minimizing the angle between the

153   spindle axis and the **b**-axis with the operations of the goniometer arcs represented as rotation

154   matrices. In Figure 3, open circles represent the orientation after the goniometer arcs are adjusted

155   so that Y = **b** is parallel to the spindle axis (the -x, +x cartesian axis); this required an up-arc

156   adjustment of -10.7° and lo-arc adjustment of -0.2° in this example. The beamline geometry is

157   then adjusted to match the microscope cartesian basis.

158   Fe K-edge spectra were collected at the 13-ID-E undulator-based microprobe at the

159   GeoSoilEnviro-CARS sector, Advanced Photon Source (APS), Argonne National Laboratory,

160   USA. Optical and instrument configuration of the beamline is outlined in Sutton et al. (2017). A

161 cryogenically-cooled, double-crystal Si(311) monochromator set was used for monochromatic

162 radiation. Beam to sample focusing was performed using a pair of 240 mm long, polished,

163 dynamically-bent silicon mirrors in a Kirkpatrick-Baez (KB) geometry. Beam focus is capable of

164 generating focused spot sizes of approximately 1.5 x 2 μm full-width half maximum, and

165 incident monochromatic flux (I_0) in excess of 6 x 10^{12} photons/second, which is measured in a

166 helium-filled, 200 mm-long ion chamber upstream of KB mirror optics.

167   Experiments from this research measured fluorescence with a solid-state detector at 90°

168 to the X-ray source axis (Figure 2). Fluorescence spectra were collected using a Canberra SXD-7

169 7 element Si drift detector in conjunction with the high-speed digital spectrometer system

170 Quantum Xpress3. Incident X-ray energy was calibrated on the first derivative peak of Fe,

171 7110.75 eV, from an Fe metal foil standard (Kraft et al., 1996) and no energy drift was detected

172 throughout the analytical session. X-ray absorption spectra were collected for fluorescence with

173 a collection time of 1 second per step from 7012 to 7104 eV at an energy increment of 2 eV from

174 7012 to 7104 eV for the background region, 0.1 eV increment from 7104 to 7124 eV for the pre-

175 edge and edge region, 0.5 eV increment from 7124 to 7152 eV for the near edge region, and 5 eV

176 increment 7152 to 7407 eV for the EXAFS region.

177   A motorized θ-axis and ϕ-axis stage were used to perform the microscope stage and

178 spindle stage rotations to align vectors parallel to the **{{typesetting, here and elsewhere, the**

179 **arrow goes above the E}}**$\vec{E}$ field vector, though the wave vector direction $\vec{k}$ is also known for

180 each crystal (Figure 2). Spectra were normalized and flattened initially in the software Larch

181 (Newville, 2013), and figures of the pre-edge are renormalized near the pre-edge to reduce the

182 effects of overabsorption outliers and focus on anisotropy. Flattened full spectra from 7012 to

183 7354 eV from this research are provided in the Online Materials[1].

184

Fitting Data

186

Above the pre-edge, anisotropy of XAS is well-characterized as a $\cos^2\theta$ or $\cos^2\phi$ relationship from one absorption magnitude to another, as is the case for other absorption spectroscopies (Steven et al., 2022). However, pre-edge peaks are attributed to quadrupole and mixed quadrupole-dipole transitions (De Groot et al., 2009). Because of the quadrupole contributions, interpolating absorption anisotropy in the pre-edge requires a different model. The angular-dependence of quadrupole transitions with respect to ϕ is fit by $1-\cos4\phi$ following Hahn et al. (1982) and Uozumi et al. (1992). Note that in their experiments, ϕ denotes the angle between $\vec{k}$ and the **a**-axis of TiO_2, where $\vec{k}$ and $\vec{E}$ are kept perpendicular to the **c**-axis. Essentially, those experiments were run by collecting spectra with the **c**-axis of TiO_2 oriented vertically and parallel to the ϕ-axis, and after rotating ϕ at several ϕ angles. The utility of running the experiment in this fashion is that the $\vec{k}$ direction relative to the crystallographic basis is easy to determine if there is angular dependence on $\vec{k}$. In the experiments for this study, ϕ only designates the angle around the axis of the spindle, and crystal orientations are designated separately. Thus, both $\vec{k}$ and $\vec{E}$ dependence are tested separately in ϕ and θ rotations.

In two dimensions, the observed $\cos^2\theta$ magnitudes of a section are fit numerically to solve the parameters a, b, and ψ in the expression $a*\cos^2(\theta + \psi) + b*\sin^2(\theta + \psi) = r$, where r is an absorption magnitude. For example, using a Gauss-Newton algorithm for angular-dependent data of spectra collected at 7120 eV, the resulting fit has the parameters a = 0.7506 b = 0.3626 ψ = 8.22° with an RMSE of 0.0136 for the sample in Figure 4. In scans where the $\cos^2$ does not fit

206   the data alone, a weighted combination of cos^2 and $1-cos4\theta$ dependences are used following the

207   discussion of mixed dipole and quadrupole absorption character in Hahn et al. (1982).

208

209   **Scan types**

210

211   Three scan types are used here to test anisotropy with respect to rotating ϕ and θ. The

212   first type includes scans where ϕ is rotated at $\theta = 0°$, which is denoted as the ϕ-axis, where $\vec{E}$ //

213   ϕ. These scans are used only to test for wave vector dependence of spectra by fixing the

214   orientation of $\vec{E}$ relative to the crystal's orientation. The second scan type is a rotation of ϕ at θ

215   $= -90°$ (ϕ-axis, $\vec{E} \perp \phi$). This geometry is inspired by visible light absorption behavior, where if

216   **b** is parallel to the ϕ-axis for a monoclinic crystal, the orthogonal direction is always a vibration

217   direction, eliminating crystal polarization effects.

218   The final scan type is a rotation of θ, which is also inspired by visible light absorption

219   behavior. This geometry is equivalent to rotating a microscope stage and observing pleochroism.

220   In θ rotations for visible light, there are two orthogonal vibration directions due to polarization

221   through the crystal. Relative to the lower polarizer, absorption magnitudes between the vibration

222   directions arise from the probability of polarization along these two paths rather than absorption

223   probability itself.

224   All three scan types were acquired on a near end-member Fe^{2+} hedenbergite sample

225   HMM119666. For the endmember Fe^{3+} aegirine samples and the mixed valence augites, only the

226   ϕ-axis, $\vec{E}$ // ϕ and ϕ-axis, $\vec{E} \perp \phi$ scans were acquired. In each geometry, a spectrum is

227   collected, then the next spectrum is collected after rotating either the ϕ-axis or θ-axis by $10°$

228   depending on scan type. This is repeated until a section spanning 0° to 170° or more is

229   completed.

230

231   **Results**

232

233   **Hedenbergite ($Fe^{3+}/\Sigma Fe = 0.0$)**

234

235   Hedenbergite samples (Fe^{2+}-containing only without Fe^{3+}) have three dominant pre-edge

236   peaks centered approximately at 7110.9 eV, 7111.7 eV, and 7113.2 eV. Hedenbergite sample

237   HMM119666 was run in three experimental geometries, two of which were sweeps with $\vec{E}$

238   oriented along various axes along (010) and one with $\vec{E}$. // ϕ-axis // **b**-axis at different angles of

239   ϕ. In the first (010) scan, the crystal was mounted with **c** // ϕ with ϕ turned such that the photon

240   propagation direction $\vec{k}$ // **b**-axis at various θ settings (Figure 2). The second (010) scan

241   geometry is with the **b**-axis // ϕ at $\theta = -90°$, while turning to various ϕ settings, and thus, $\vec{E}$ was

242   also along axes in the (010) plane.

243

244   <u>ϕ-axis, $\vec{E}$ // ϕ // **b**-axis</u>

245

246   The ϕ-axis scan with $\vec{E}$. // ϕ // **b**-axis was run to test if or to what degree is there wave

247   vector dependence of X-ray absorption spectra of clinopyroxenes. HMM119666 was mounted

248   with the spindle axis ϕ parallel to the **b**-axis for both consistency and to cover a wide variety of

249   orientations relative to a known symmetry axis. The scan geometry of this experiment has θ

250   fixed at zero for all spectra with the spindle axis parallel to the polarization axis $\vec{E}$. Spectra

251   were collected every 10 degrees from $\phi = 0°$ to $\phi = 170°$. With $\vec{E}$ fixed along the b-axis, the

252   angular dependence of absorption relative to the crystal's orientation is with respect to $\vec{k}$

253   orientation in this dataset (Figure 6). As demonstrated in Figure 6, pre-edge peaks of

254   hedenbergite have strong absorption anisotropy when $\vec{k}$ is varied and the orientation of $\vec{E}$ is

255   fixed relative to the crystal. Spectra are fit with a $\cos^2\phi$ dependence for comparison, based on its

256   coincidence with the data.

257

258   <u>θ-axis, $\vec{E} \perp$ **b**-axis</u>

259

260   Absorption magnitudes collected at different settings of θ were used to test whether

261   absorption anisotropy at X-ray wavelengths is analogous to UV-Vis and infrared wavelengths.

262   This geometry is equivalent to observing absorption magnitudes by rotating the microscope stage

263   of a pleochroic mineral in thin section. In this set of experiments, a single crystal of HMM19666

264   was mounted with the **c**-axis parallel to the φ-axis and φ was rotated to make $\vec{k}$ parallel to the **b-**

265   axis at each θ setting. The resulting absorption magnitudes of the prominent pre-edge peaks are

266   plotted relative to θ setting in Figure 7 and fit with $\cos^2\theta$ dependence for comparison. After

267   normalizing, observed absorption anisotropy closely correspond to the $\cos^2\theta$ model for all

268   energies, and the angular dependence of the prominent peak centroids are plotted radially in

269   Figure 7.

270

271   <u>φ-axis, $\vec{E} \perp \phi$</u>

272

273   The geometry of scans where ϕ is rotated at $\theta = -90°$ is depicted in Figure 2. In this

274   geometry, the **b**-axis of HMM119666 is mounted parallel to the ϕ-axis and resulted in the

275   absorption magnitudes shown in Figure 8. The orientations of both $\vec{k}$ and $\vec{E}$ are varied relative

276   to the crystallographic orientation. They result in a lobed absorption anisotropy relative to the

277   rotation axis minimum and maximum absorption occurring at 45° to one another with respect to

278   $\vec{k}$ and $\vec{E}$. Only the 7113.2 eV peak can be fit with the 1-cos4ϕ model. The other two peaks are

279   fit with a mixed model using weighted components of both 1-cos4ϕ and cos$^2\phi$ for comparison.

280

281   **Augite ($Fe^{3+}/\Sigma Fe = 0.36$)**

282

283   An intermediate $Fe^{3+}/\Sigma Fe$ concentration of augite, DH208, was analyzed to assess pre-

284   edge peak intensities of a common composition of clinopyroxene. The pre-edge peaks of DH208

285   is subdivided into centroids centered at 7111.2 eV, 7112.9 eV, 7114.1 eV (Figure 9). Spectra of

286   augite were only collected in the geometry where ϕ is rotated with $\vec{E}$ perpendicular to ϕ at a

287   fixed θ position of -90°. This corresponds to the exact position from Figure 2 and collecting

288   spectra every 10° from 0-170° ϕ. As with the pre-edge absorption of hedenbergite, augite spectra

289   also have the lobed absorption anisotropy when analyzed in this geometry. The peak centered at

290   7111.2 eV has absorption magnitudes with stronger four-fold symmetry, similar to the 7113.2 eV

291   peak of HMM119666. The 7112.9 eV and 7114.1 eV peaks are not as anisotropic as the 7111.eV

292   peak, but do exhibit nonsystematic differences in absorption intensity when normalized to 7115.5

293   eV. Peaks are fit with combined cos$^2\phi$ and 1-cos4ϕ models due to the large discrepancy with

294   both models when applied individually.

295

296 **Aegirine ($Fe^{3+}/\Sigma Fe = 0.97$)**

297

298   Aegirine samples that are completely oxidized consistently have two dominant pre-edge

299 peaks, one centered at 7112.8 eV and the other centered near 7114.1 eV. Among trivalent

300 transition metal oxides, the general interpretation of the lowest energy peak is that it arises from

301 quadrupole transitions to the empty d orbital. The next higher-energy peak has differing

302 interpretations, but is thought to occur from a mix of quadrupole transitions to $3d$ orbital and

303 non-local excitations to an adjacent $4p$ orbital (Vanko et al., 2008). In both scan geometries

304 analyzed, aegirine exhibits the greatest difference in absorption extremes of the pre-edge peaks

305 in all pyroxenes scanned when comparing Figures 6 - 11.

306

307 $\underline{\phi\text{-axis, } \vec{E} \text{ // } \phi}$

308

309   A limited dataset was collected in the geometry in which $\vec{E}$ // ϕ // **b**-axis to investigate

310 whether or not the anisotropy of the Fe^{3+} end-member aegirine is similar to the Fe^{2+} hedenbergite

311 sample. Absorption magnitudes are plotted radially and fit with a $\cos^2\phi$ model in Figure 10. Even

312 with the limited dataset, absorption magnitudes also follow the $\cos^2\phi$ model as with the more-

313 complete dataset of HMM119666. At a minimum, this dataset demonstrates strong absorption

314 anisotropy, and the angular dependence of the absorption anisotropy does not have four-fold

315 symmetry, just as with HMM119666 in this geometry.

316

317 $\underline{\phi\text{-axis, } \vec{E} \perp \phi}$

318

319   The 7112.8 eV aegirine peak collected in the ϕ-axis, $\vec{E} \perp \phi$ geometry resembles the

320   same lobed appearance as the 7113.2 eV peak of hedenbergite and the 7111.2 eV peak of augite

321   (Figure 11). The 7114.1 eV peak is only similar to the 7114.1 eV peak of augite but is not

322   particularly well described by either the $\cos^2\phi$ or $1\text{-}\cos4\phi$ models individually. Rather, a mixed

323   model is applied to fit the datapoints following the discussion of mixed quadrupole and dipole

324   transition character among trivalent oxides in Vanko et al. (2008). The pre-edge peaks of

325   aegirine are both the most intense, and most anisotropic in terms of the variation of peak area

326   ratio differences between the 7112.8 and 7114.1 eV peaks with respect to ϕ position.

327

328   **Discussion**

329

330   Individually, wave vector dependence appears to be the same as field vector dependence,

331   in that absorption anisotropy is well-fit with the $\cos^2$ model. However, when varying both the

332   wave vector and field vector orientations of any pyroxene crystal, absorption magnitudes

333   delineate irregular patterns that do not always correspond with the $1\text{-}\cos4\phi$ model that worked to

334   describe anisotropy in TiO_2 from Uozumi et al. (1992). Arguably, the combination of the two

335   models describes the absorption anisotropy from Figures 8, 9, and 11 that would coincide with

336   the explanation of mixed dipole and quadrupole character from each sample. Scans analyzing the

337   same section, such as the (010) of HMM119666, exhibit different results depending on rotation

338   and mount axis. For example, with $\vec{E}$ in the (010) plane, absorption magnitudes collected by

339   rotating ϕ (Figure 8) differs from those collected by rotating θ (Figure 7). This suggests that

340   quadrupole transitions are also strongly dependent on $\vec{k}$ orientation unlike dipole transitions

341   (Hahn et al., 1982). The results from this study, particularly the scans from HMM119666 are

342 antithetical to the expected absorption anisotropy if pre-edge peaks resulted from dipole

343 transitions alone. With the selection rules of quadrupole transitions having dependence on $\vec{E}$

344 and $\vec{k}$ orientation (Hahn et al., 1982), the exact scan geometry of the pre-edge is thus a

345 significant factor when analyzing the pre-edge of anisotropic crystals.

346   Absorption above pre-edge energies does not demonstrate significant variation with

347 respect to $\vec{k}$ orientation alone (Figure 5). However, the systematic difference in absorption due

348 to differing count rates for each spectrum collected in Figure 5 emphasizes another concern. This

349 concern is the extreme sensitivity of the rising edge to thickness and absorber concentration as

350 discussed in Heald and Stern (1977). Ordinarily, corrections for variation in count rates produce

351 consistent results for multiple spectra collected on irregular crystals. However, overabsorption is

352 likely when analyzing thicker sections of irregular, high Fe crystals such as hedenbergite. As a

353 result, the peaks just above the rising edge are vary in scale, though in a systematic way.

354

355 <u>Comparisons between visible light and X-ray absorption</u>

356

357   Absorption anisotropy in the pre-edge is only similar to visible light anisotropy in two

358 ways. The first is that rotations around the wave vector axis result in $\cos^2\theta$ dependence of

359 absorption magnitudes. The second similarity is that the pre-edge absorption anisotropy has

360 wave vector orientation dependence. With visible light, this dependence arises from the

361 polarization paths through the crystal, whereas with X-ray wavelengths, the dependence is

362 related to differences in atomic positions along the propagation path, along with the type and

363 nature of the transitions.

364   When changing the propagation path at a fixed vibration path orientation, there are no

365   perceivable differences in absorption intensity above pre-edge energies. In contrast, pre-edge

366   peak intensities vary by as much as 33% of its maximum intensity when changing the

367   propagation path, even at a fixed $\vec{E}$ orientation. In visible light spectroscopy, a change in

368   absorption due to propagation path orientation does occur, but is understood to be due to a

369   change in polarization state through the crystal. Because anisotropic crystals are considered to

370   split visible light into two linear vibration paths in classical mechanics, the amount of absorption

371   depends on the amount of light traveling along each path, and the amount of absorption along

372   each path. The amount of light traveling along each path depends on the initial orientation of

373   linearly polarized light relative to the orientations of the two vibration paths. In the XAS

374   experiments above, fluorescence is measured and is proportional to absorption. The disparity

375   between visible light and X-ray absorption anisotropy is strongest when examining pre-edge

376   energies and is only apparent in geometry from Figure 2 where ϕ is rotated. Rotations of ϕ with

377   the rotation axis parallel to the polarization axis at pre-edge energies result in $\cos^2$ angular-

378   dependence. Similarly, rotations of θ also have the $\cos^2$ dependence between pre-edge energies

379   and visible light. As mentioned, the disparity arises from the geometry where ϕ is rotated and $\vec{E}$

380   is orthogonal to the ϕ-axis and propagation direction. When modeling the effects of polarization

381   with the optical indicatrix model combined with an absorption indicatrix model of a monoclinic

382   crystal, rotations of ϕ do not result in absorption magnitudes with four-fold symmetry.

383   Under visible light, ϕ rotations with the geometry of Figure 2 will have two-fold

384   symmetry angular-dependence rather than the four-fold symmetry shown in Figures 8, 9, and 11.

385   Depending on how the crystal is mounted, lower symmetry crystals will generally display two-

386   fold angular-dependence of absorption, which is not necessarily $\cos^2$ dependent in this geometry.

387

Possible factors contributing to X-ray absorption anisotropy

389

390   At X-ray wavelengths, diffraction dominates, which has a significant effect on X-ray

391   absorption. For example, the Borrmann effect is the increased X-ray transparency of a crystal

392   along Bragg reflections (Borrmann, 1941).

393   Moreover, quadrupole transitions of the pre-edge have different angular dependence of

394   absorption probabilities than dipole transitions both in theory and observation. As mentioned

395   above, the fits of the pre-edge by Uozumi et al. (1992) from Ti K-edge spectra use the $1-\cos4\phi$

396   model. This model fits some of the pre-edge peaks of pyroxenes but not all. It should also be

397   noted that ϕ only refers to the experimental geometry, so the equation is not necessarily

398   applicable to field vector orientations in the crystal's basis. Rather, it may depend on how the

399   crystal is mounted. As shown in Figures 7 and 8, collecting absorption spectra with the field

400   vector oriented along the same axes with differing wave vector directions may yield different

401   results.

402   If X-ray absorption anisotropy was dependent only on the field vector orientation relative

403   to absorbers, there should be no difference in the results shown in Figures 7 and 8, nor should

404   there be variation in the spectra from Figure 10. Further, wave vector dependence is distinct only

405   in the pre-edge of spectra. Differences of absorption anisotropy between quadrupole and dipole

406   transitions are likely the reason for the strong dependence of $\vec{k}$ orientation for pre-edge

407   energies.

408

$1-\cos4\phi$ dependence

410

411   The lobed anisotropy that arises only from the ϕ-axis, $\vec{E} \perp \phi$ experiments apparently

412   results from the combined wave vector and field vector dependences of the spectra. When

413   spectra are collected at different ϕ-axis settings at $\phi = 0$, however, the orientation of $\vec{E}$ is fixed

414   and the anisotropy follows the $\cos^2$ model. With our limited dataset testing the wave vector

415   dependence of the pre-edge, the absorption magnitudes do not resemble the lobed appearance of

416   the other ϕ-axis scans, and instead correspond closely with the $\cos^2\phi$ fit.

417   Wave vector dependence may arise from a change in multiple scattering paths. In θ

418   rotations, multiple scattering paths are the same relative to the wave vector. Although numerous

419   authors have demonstrated absorption anisotropy of XAS, wave vector and field vector

420   dependence of pre-edge XAS anisotropy was theorized by Brouder (1990) on the basis of

421   multiple-scattering theory combined with group theory.

422   Regardless of whether the wave vector dependence is due to the nature of the quadrupole

423   transitions or a product of multiple scattering paths, the pre-edge is significantly affected by both

424   the orientation of the wave vector and field vector. In experiments where the field vector

425   orientation was fixed and wave vector varied, absorption intensity changed by as much as 33%.

426   This implies that empirical quantification of valence states of anisotropic crystals using the pre-

427   edge is far more complicated than originally thought. Reference datasets for determining redox

428   ratios in anisotropic crystals must account for both contributors to anisotropy. This involves

429   either modeling the anisotropy, or, creating a dataset that is valid for a specific orientation, both

430   in section, and vibration direction.

431

432   **Implications**

433

434   Given the significant wave vector and field vector orientation dependence of XAS on

435 pyroxenes, absorption anisotropy remains difficult to characterize. The fact that anisotropy with

436 respect to wave vector orientation is just as significant as field vector orientation implies that

437 orientation-dependent XAS studies will be most useful if they keep track of $\vec{E}$ and $\vec{k}$ in the

438 crystal's basis for each spectrum. The uncertainty of how absorption magnitudes are influenced

439 by orientation has major ramifications for quantifying valence states using the pre-edge only,

440 even in studies attempting to compare similar orientations. In this regard, collecting a spectrum

441 along the same orientation generally refers to the orientation of the field vector, though in XAS,

442 the wave vector axis must also be the same to eliminate the orientation variable in a valence state

443 calibration. Given the change in peak intensity by 33% in some pre-edge peaks, this can

444 dramatically influence Fe valence state predictions in clinopyroxene based on the pre-edge alone,

445 especially if the analyzed orientation does not have the exact same $\vec{E}$ and $\vec{k}$ orientation in the

446 crystal's basis. The clinopyroxene group minerals studied here are an extreme example of

447 absorption anisotropy due to the linear arrangement of the absorbers in their structure.

448   More optimistically, this study provides the first steps that will enable modeling for

449 valence state calibrations in pyroxenes empirically. Anisotropy from rising edge energies up

450 follow straightforward systematics once enough datapoints are collected to define characteristic

451 absorption axes (Steven et al., 2022). This allows production of a database of spectra, collected

452 at all possible orientations, to be built from oriented spectra of standards with known Fe^{3+}

453 contents. In other words, acquisition of XAS spectra from standards with known Fe^{2+} and Fe^{3+}

454 concentrations at known orientations provides the data from which spectra at any orientation can

455 now be calculated. Those data can in turn be used as training data for classification or regression

456   models utilizing machine learning algorithms. The resultant models can be used to predict Fe^{2+}

457   and Fe^{3+} in unknown samples at random orientations, either by matching spectra of unknowns to

458   those of standards, or through multivariate analyses based on the training data. Our group is

459   pursuing this approach for pyroxenes, with an ultimate goal of generating robust methodology

460   for measuring Fe^{2+} and Fe^{3+} in pyroxenes in thin section.

461

462   **Funding**

463

466

467   **References**

468

469   Bajt, S., Sutton, S.R., and Delaney, J.S. (1994). X-ray microprobe analysis of iron oxidation

470   states in silicates and oxides using X-ray absorption near edge structure

471   (XANES). Geochimica et Cosmochimica Acta, 58(23), 5209-5214.

472   Borrmann, G. (1941). Über Extinktionsdiagramme der Röntgenstrahlen von Quarz.

473   Physikalische Zeitschrift, 42, 157-162.

474   Brouder, C. (1990). Angular dependence of X-ray absorption spectra. Journal of Physics:

475   Condensed Matter, 2(3), 701.

476   De Groot, F., Vankó, G., and Glatzel, P. (2009). The 1s x-ray absorption pre-edge structures in

477   transition metal oxides. Journal of Physics: Condensed Matter, 21(10), 104207.

478   Dyar, M.D., Gunter, M.E., Delaney, J.S., Lanzarotti, A., and Sutton, S.R. (2002). Systematics in

479   the structure and XANES spectra of pyroxenes, amphiboles, and micas as derived from

480   oriented single crystals. The Canadian Mineralogist, 40(5), 1375-1393.

481   Gendzwill, D.J., and Stauffer, M.R. (1981). Analysis of triaxial ellipsoids: Their shapes,

482   plane sections, and plane projections. Journal of the International Association for

483   Mathematical Geology, 13(2), 135-152.

484   Glatzel, P., Mirone, A., Eeckhout, S.G., Sikora, M., and Giuli, G. (2008). Orbital

485   hybridization and spin polarization in the resonant 1s photoexcitations of

486          $\alpha-Fe_2O_3$. Physical Review B, 77(11), 115133.

487   Hahn, J.E., Scott, R.A., Hodgson, K.O., Doniach, S., Desjardins, S.R., and Solomon, E.I.

488   (1982). Observation of an electric quadrupole transition in the X-ray absorption spectrum

489   of a Cu (II) complex. Chemical Physics Letters, 88(6), 595-598.

490   Heald, S.M., and Stern, E.A. (1977). Anisotropic X-ray absorption in layered

491   compounds. Physical Review B, 16(12), 5549.

492   Kraft, S., Stümpel, J., Becker, P., and Kuetgens, U. (1996). High resolution x-ray absorption

493   spectroscopy with absolute energy calibration for the determination of absorption edge

494   energies. Review of scientific instruments, 67(3), 681-687.

495   Libowitzky, E., and Rossman, G.R. (1996). Principles of quantitative absorbance measurements

496   in anisotropic crystals. Physics and Chemistry of Minerals, 23(6), 319-327.

497

498   Muñoz, M., Vidal, O., Marcaillou, C., Pascarelli, S., Mathon, O., and Farges, F. (2013). Iron

499   oxidation state in phyllosilicate single crystals using Fe-K pre-edge and XANES

500   spectroscopy: Effects of the linear polarization of the synchrotron X-ray beam. American

501   Mineralogist, 98(7), 1187-1197.

502   Newville, M. (2013). Larch: an analysis package for XAFS and related spectroscopies. In J Phys

503   Conf Ser (Vol. 430, p. 012007).

504   Rosenberg, R.A., Love, P.J., and Rehn, V. (1986). Polarization-dependent C (K) near-edge x-

505   ray-absorption fine structure of graphite. Physical Review B, 33(6), 4034.

506   Steven, C.J., Dyar, M.D., McCanta, M., Newville, M., and Lanzirotti, A. (2022). The absorption

507   indicatrix as an empirical model to describe anisotropy in X-ray absorption spectra of

508   pyroxenes. American Mineralogist: Journal of Earth and Planetary Materials, 107(4),

509   654-663.

510   Steven, C.J., and Gunter, M.E. (2020). EXCALIBR to EXCELIBR and the optical

511   orientation of minerals: Correcting the optical orientation of clinoamphiboles. American

512   Mineralogist: Journal of Earth and Planetary Materials, 105(6), 955-962.

513   Steven, C.J., and Gunter M.E. (2017). EXCELIBR: An Excel Spreadsheet for Solving the

514   Optical Orientation of Uniaxial and Biaxial Crystals. The Microscope 65 (4), 147-152.

515   Stöhr, J., and Outka, D.A. (1987). Determination of molecular orientations on surfaces from the

516   angular dependence of near-edge x-ray-absorption fine-structure spectra. Physical

517   Review B, 36(15), 7891.

518   Sutton, S.R., Lanzirotti, A., Newville, M., Rivers, M.L., Eng, P., and Lefticariu, L. (2017).

519   Spatially resolved elemental analysis, spectroscopy and diffraction at the GSECARS

520   sector at the advanced photon source. Journal of environmental quality, 46(6), 1158-

521   1165.

522   Uozumi, T., Okada, K., Kotani, A., Durmeyer, O., Kappler, J.P., Beaurepaire, E., and

523   Parlebas, J.C. (1992). Experimental and theoretical investigation of the pre-peaks at the

524   Ti K-edge absorption spectra in TiO_2. EPL (Europhysics Letters), 18(1), 85.

525   Vankó, G., de Groot, F.M., Huotari, S., Cava, R. J., Lorenz, T., and Reuther, M. (2008).

526   Intersite 4p-3d hybridization in cobalt oxides: a resonant x-ray emission spectroscopy

527   study. arXiv preprint arXiv:0802.2744.

528   Wilke, M., Partzsch, G.M., Bernhardt, R., and Lattard, D. (2004). Determination of the iron

529   oxidation state in basaltic glasses using XANES at the K-edge. Chemical

530   Geology, 213(1-3), 71-87.

531   Yaxley, G.M., Berry, A.J., Kamenetsky, V.S., Woodland, A.B., and Golovin, A.V. (2012).

532   An oxygen fugacity profile through the Siberian Craton—Fe K-edge XANES

533   determinations of $Fe^{3+}/\sum Fe$ in garnets in peridotite xenoliths from the Udachnaya East

534   kimberlite. Lithos, 140, 142-151.

535

554   **Figures**

555
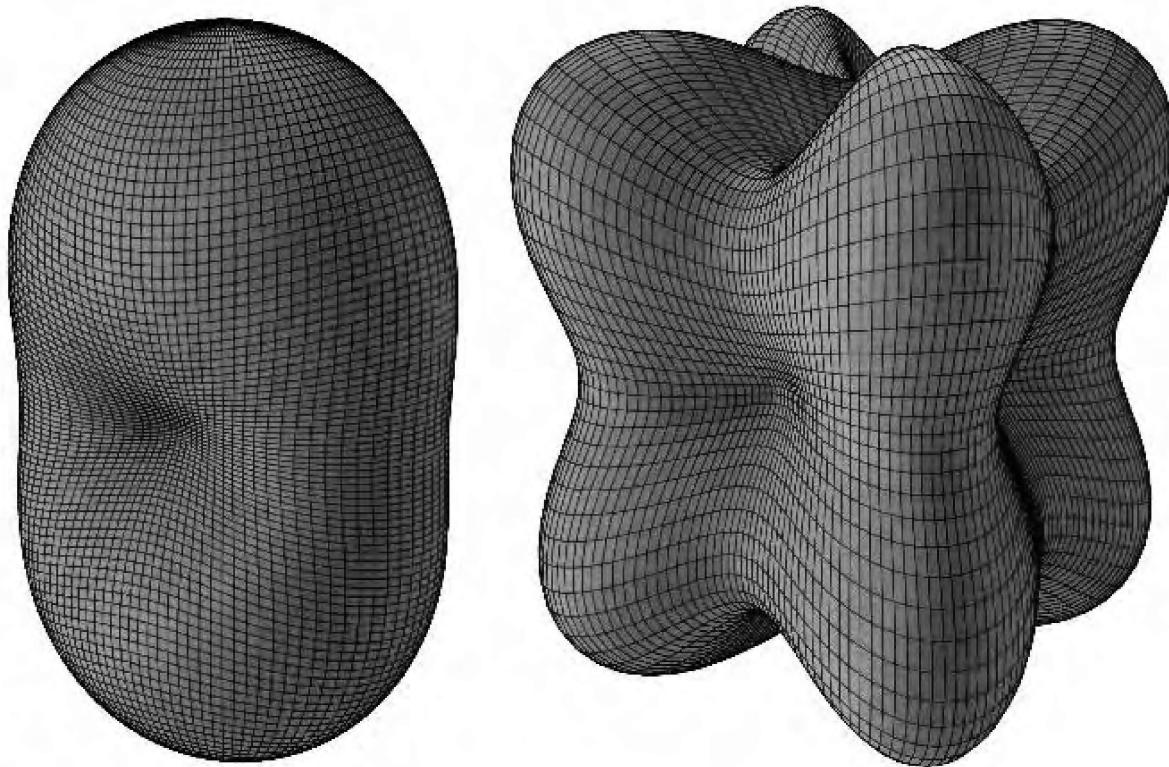
556

557   **Figure 1)** Absorption indicatrices based on absorption due to only dipole transitions (left) and a

558   possible absorption indicatrix due to quadrupole transitions (right).

559

560
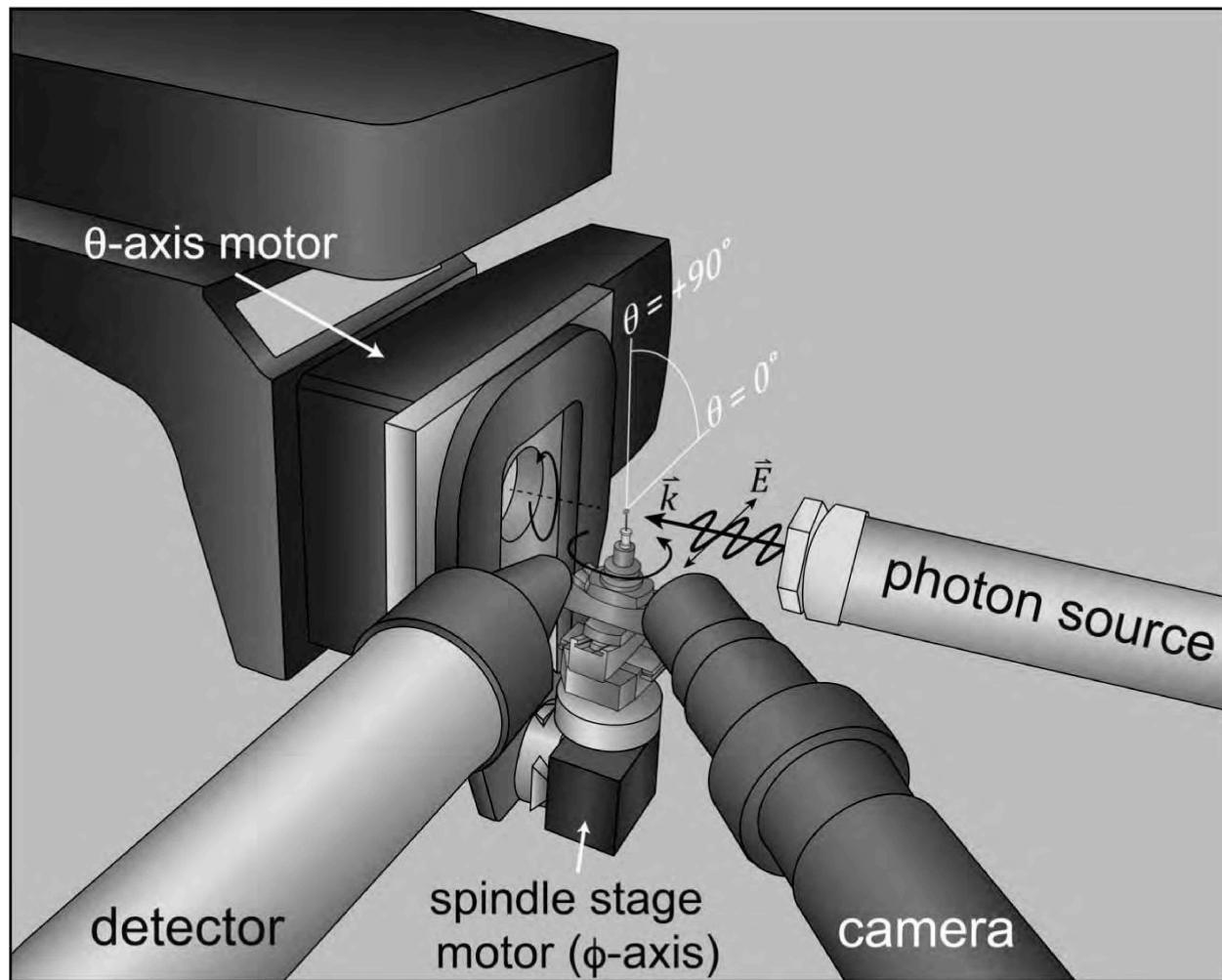
Figure 2) Experimental geometry for analyzing single crystals at Argonne National Laboratory.

A motorized spindle ϕ and stage θ rotate around their respective axes. The wave vector $\vec{k}$ of the

photon source propagates along the θ-axis and the field vector $\vec{E}$ is orthogonal to $\vec{k}$ and in the

horizontal plane.
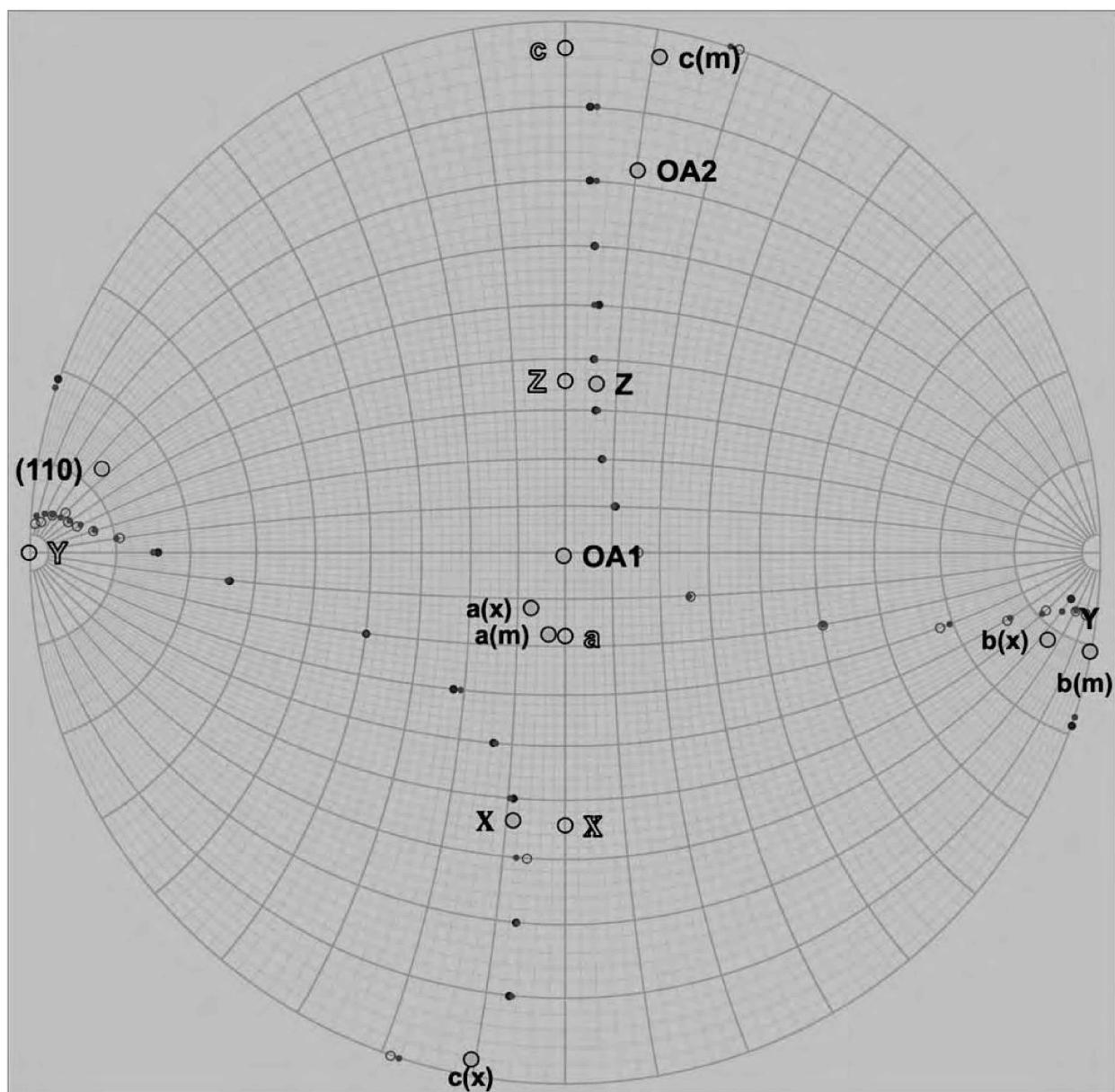
566
567 **Figure 3)** Stereogram of an initial determination of principle optical vectors and crystallographic
568 axes of a pyroxene. The orientation after manipulating the goniometer arcs is represented as open
569 circles.
570
571
572
573

574
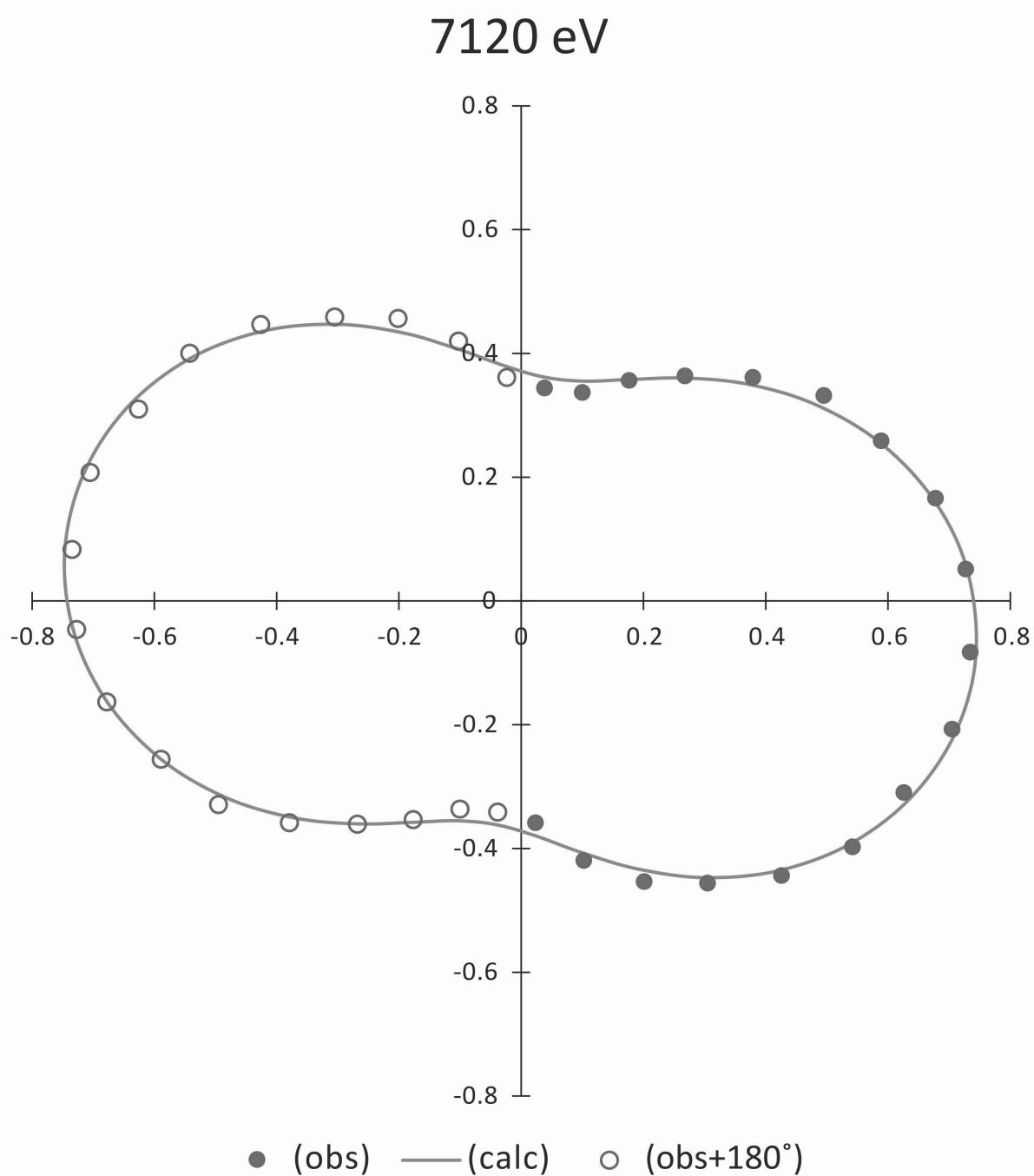
Figure 4) Absorption magnitudes collected at the rising edge (7120 eV) with $\vec{E}$ oriented along

various axes in the (010) plane of a 34% $Fe^{3+}/\Sigma Fe$ augite. In this and following figures, the

magnitudes of the axes represent absorption intensity.

578

579

580
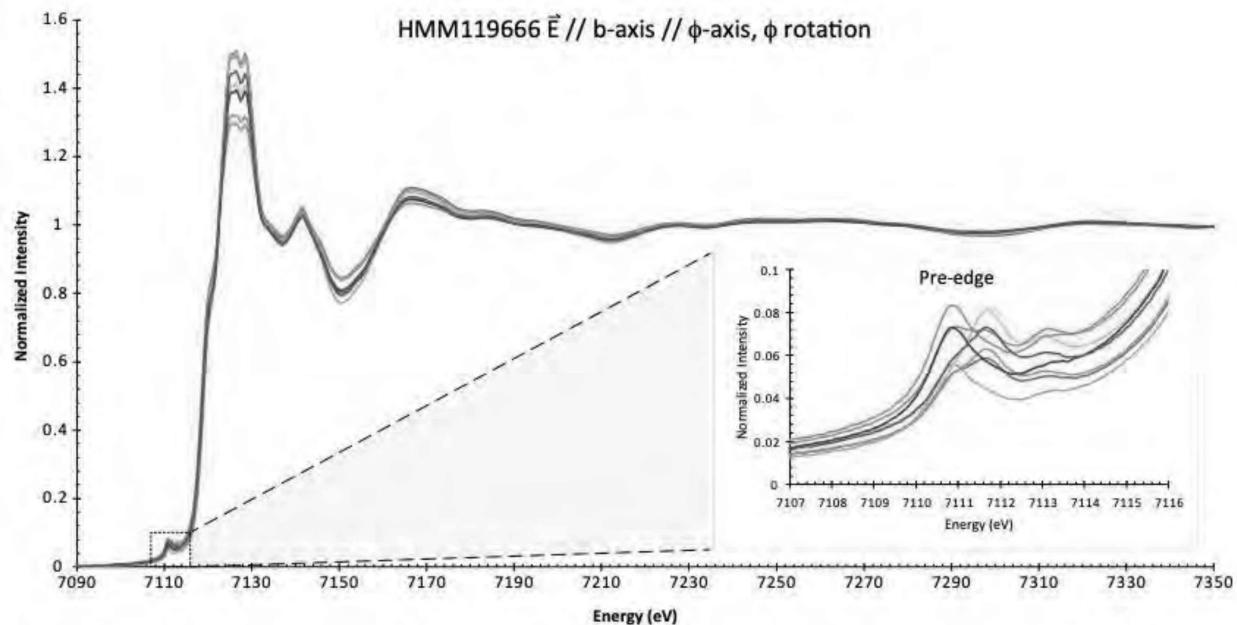
581
582 **Figure 5)** Full X-ray absorption spectra collected from multiple wave vector axes with the field
583 vector axis fixed. A plot of a magnified view of the pre-edge is inset, and a detailed examination
584 of the anisotropy of the pre-edge peak centroids for this sample is given in Figure 6.

585
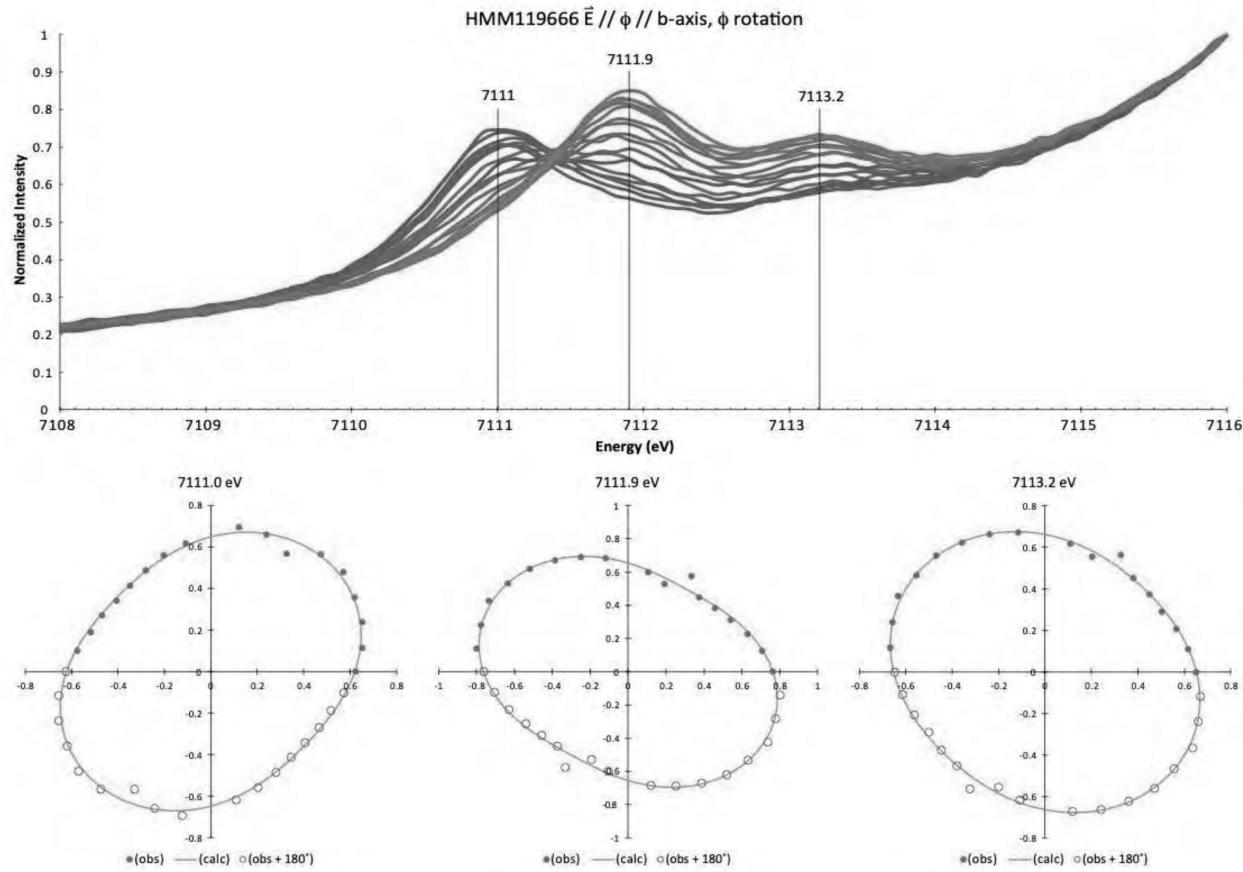
586

587 **Figure 6)** X-ray absorption spectra (top) of a 0.0 $Fe^{3+}/\Sigma Fe$ hedenbergite analyzed at a selection

588 of ϕ-axis angles with $\vec{E}$ // ϕ // **b**-axis. The resulting absorption magnitudes are plotted radially

589 with respect to $\vec{k}$ orientation (bottom) at 7110.8, 7111.7, and 7113.1 eV. Absorption magnitudes

590 are the distances of the points from the origin in the radial plots, and are fit with $\cos^2\phi$ for

591 comparison. Axes in bottom row follow conventions used in Figure 4.

592

593

594
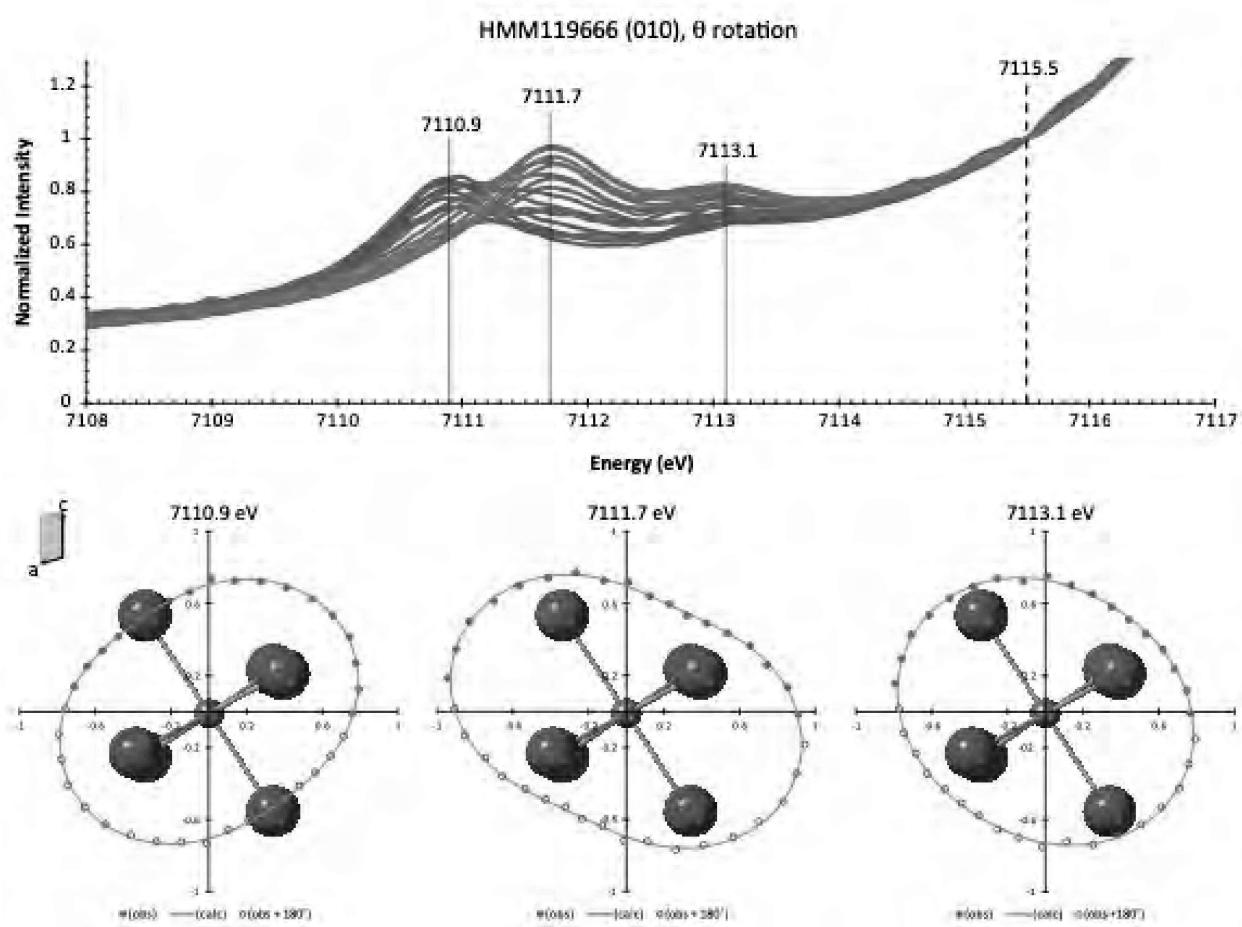
Figure 7) X-ray absorption spectra (top) of a 0.0 Fe^{3+}/ΣFe hedenbergite analyzed with $\vec{E}$ oriented along various axes in (010) with the orientation of $\vec{k}$ fixed along the b-axis. Absorption magnitudes are plotted radially (bottom) with respect to the orientation of $\vec{E}$ at 7110.9, 7111.7, and 7113.1 eV. Spectra are renormalized near the pre-edge peaks at 7115.5 eV to highlight the anisotropy. The orientation of the crystallographic axes and the coordinating polyhedron of the M1 site is depicted relative to the orientation of the absorption magnitudes. Axes in bottom row follow conventions used in Figure 4.

HMM119666 (010) φ rotation
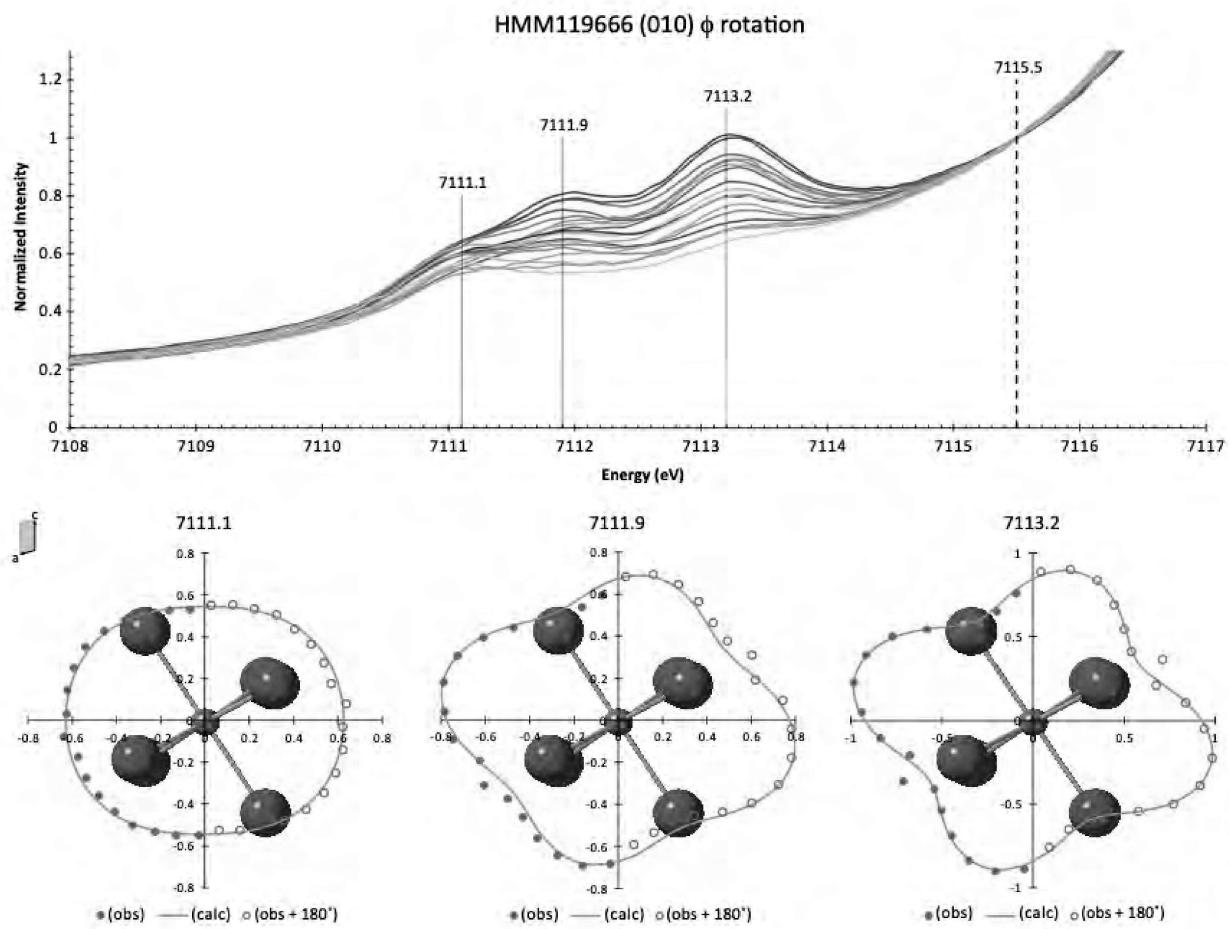
Figure 8) X-ray absorption spectra (top) of a 0.0 $Fe^{3+}/\Sigma Fe$ hedenbergite analyzed with $\vec{E}$ and $\vec{k}$ oriented along various axes in (010). The crystal was mounted with the b-axis // φ-axis at θ = -90° as depicted in Figure 2 with spectra collected at various φ settings. Absorption magnitudes are plotted radially with respect to $\vec{E}$ orientation, and for each datapoint the orientation of $\vec{k}$ is 90° away. Spectra are renormalized near the pre-edge peaks at 7115.5 eV to highlight the anisotropy. The orientation of the crystallographic axes and the coordinating polyhedron of the M1 site is depicted relative to the orientation of the absorption magnitudes. Axes in bottom row follow conventions used in Figure 4.

Figure 9) X-ray absorption spectra (top) of a 0.3 $Fe^{3+}/\Sigma Fe$ augite analyzed with $\vec{E}$ and $\vec{k}$ oriented along various axes in (010). The crystal was mounted with the b-axis // ϕ-axis at $\theta = -90°$ as depicted in Figure 2 with spectra collected at various ϕ settings. Absorption magnitudes are plotted radially with respect to $\vec{E}$ orientation, and for each datapoint the orientation of $\vec{k}$ is 90° away. Spectra are renormalized near the pre-edge peaks at 7115.5 eV to highlight the anisotropy. The orientation of the crystallographic axes and the coordinating polyhedron of the M1 site is depicted relative to the orientation of the absorption magnitudes. Axes in bottom row follow conventions used in Figure 4.

623

624

625   **Figure 10)** X-ray absorption spectra (top) of a 1.0 $Fe^{3+}/\Sigma Fe$ aegirine analyzed at a selection of ϕ-

626   axis angles with $\vec{E}$ // ϕ // **b**-axis. The resulting absorption magnitudes are plotted radially with

627   respect to $\vec{k}$ orientation (bottom) at 7112.9 and 7114.2 eV. Absorption magnitudes are fit with

628    $\cos^2\phi$ for comparison. Axes in bottom row follow conventions used in Figure 4.
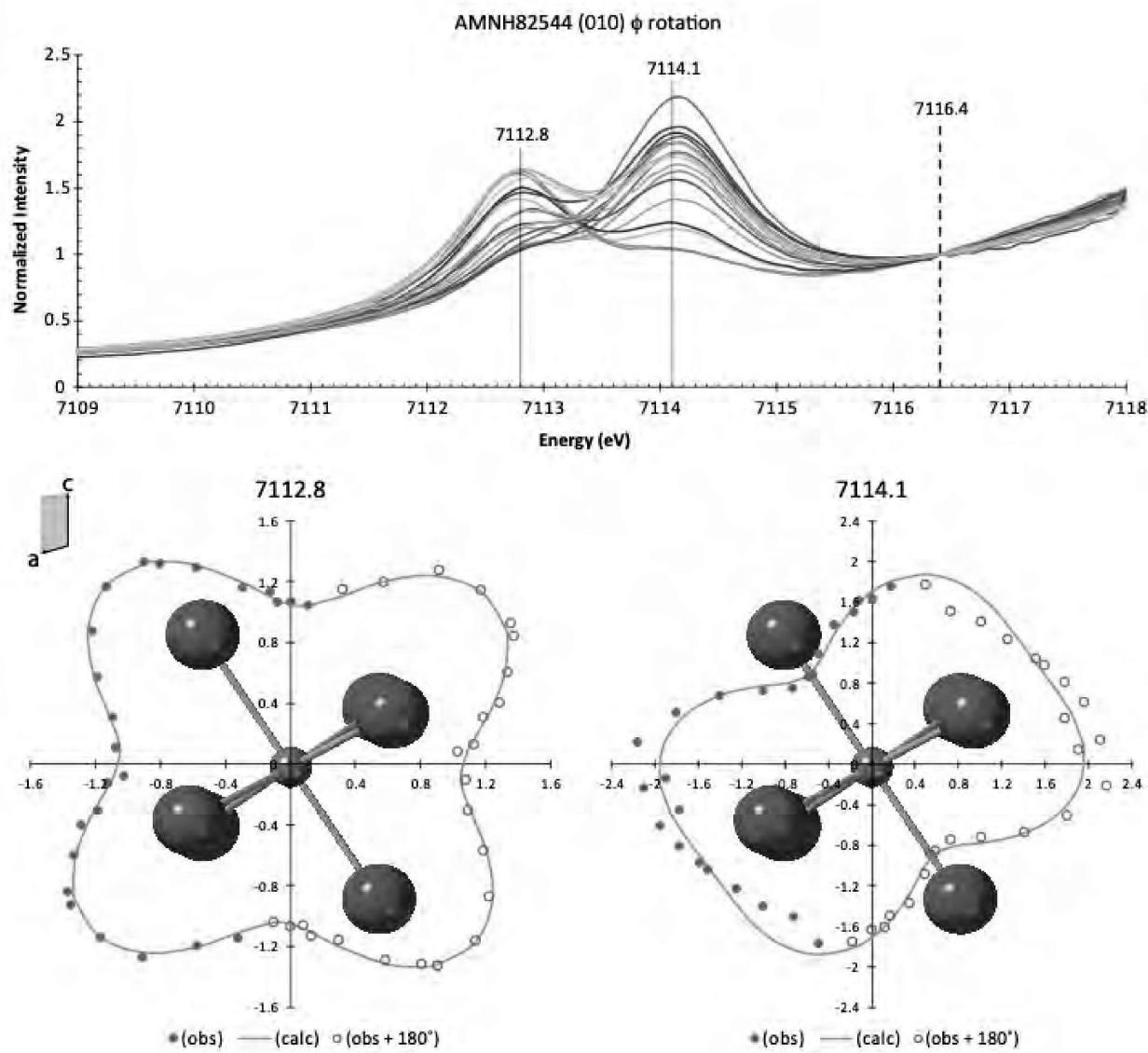
629

630 **Figure 11)** X-ray absorption spectra (top) of a 1.0 $Fe^{3+}/\Sigma Fe$ aegirine analyzed with $\vec{E}$ and $\vec{k}$

631 oriented along various axes in (010). The crystal was mounted with the b-axis // ϕ-axis at $\theta = -$

632 90° as depicted in Figure 2 with spectra collected at various ϕ settings. Absorption magnitudes

633 are plotted radially with respect to $\vec{E}$ orientation, and for each datapoint the orientation of $\vec{k}$ is

634 90° away. Spectra are renormalized near the pre-edge peaks at 7116.4 eV to highlight the

635 anisotropy. The orientation of the crystallographic axes and the coordinating polyhedron of the

636 M1 site is depicted relative to the orientation of the absorption magnitudes. Axes in bottom row

637 follow conventions used in Figure 4.

638